https://doi.org/10.1038/s44406-025-00016-2

Enhancing the performance of organic solar cells and polymer light emitting diodes *via* a novel giant polyoxomolybdate bifunctional interlayer material

Jing Qiu[1], Yan Wang[1], Guofeng Wan[1], Zilong Bing[1], Huiru Liu[1], Bing Li[1], Chengzhuo Yu[1], Jinyu Zhu[1], Donal D. C. Bradley[2,3], Jingsong Huang[2] ✉, Lixin Wu[1] ✉ & Fenghong Li[1] ✉

The giant polyoxomolybdate $[(NH_4)_{42}[Mo^{VI}_{72}Mo^{V}_{60}O_{372}(CH_3COO)_{30}(H_2O)_{72}]$ {Mo_{132}} has been little used for optoelectronic device applications. In this paper we demonstrate that thin films of {Mo_{132}} and surfactant-encapsulated {Mo_{132}}, namely {Mo_{132}}-tetraoctyl ammonium (TOA) can, respectively, upshift and downshift the work functions of a variety of electrode materials, including Al, Ag and ITO, by forming suitable interface dipoles. {Mo_{132}}-TOA used as a cathode interlayer (CIL) yields a power conversion efficiency of 18% for poly[(2,6-(4,8-bis(5-(2-ethylhexyl)-4-fluorothiophen-2-yl)-benzo[1,2-b:4,5-b']dithiophene))-alt-(5,5-(1',3'-di-2-thienyl-5',7'-bis(2-ethylhexyl)benzo[1',2'-c:4',5'-c'] dithiophene-4,8-dione))] : 2,2'-((2Z,2'Z)-((12,13-bis(2-ethylhexyl)-3,9-(2-butyloctyl)-12,13-dihydro-[1,2,5]thiadiazolo[3,4-e]thieno[2",3'':4',5']thieno[2',3':4,5]pyrrolo[3,2-g]thieno[2',3':4,5]thieno[3,2-b] indole-2,10-diyl)bis(methanylylidene))bis(5,6-difluoro-3-oxo-2,3-dihydro-1H-indene-2,1-diylidene)) dimalononitrile (PM6 : L8-BO) based organic solar cells (OSCs) and a current efficiency of 15.24 cd/A in Super Yellow based polymer light-emitting diodes. In addition, OSCs using both {Mo_{132}} as anode interlayer (AIL) and {Mo_{132}}-TOA as CIL provide improved stability relative to reference devices with traditional PEDOT:PSS as AIL and poly(9,9-bis(3'-(N,N-dimethyl)-N-ethylammoinium-propyl-2,7-fluorene)-alt-2,7-(9,9-dioctylfluorene))dibromide (PFN-Br) as CIL. {Mo_{132}} thereby serves as an effective bifunctional interlayer material to optimize organic optoelectronic device performance, enhancing power conversion and light emission efficiencies and increasing lifetime.

The development of solution processed organic semiconductor optoelectronic devices has progressed from an initial focus on light emitting diodes for displays and lighting[1–3], through photovoltaic devices for solar energy harvesting and photodetection[4–6], to transistors[7,8]. It also extends to photonic devices, including polariton microcavity structures of interest for lasing and quantum phenomena[9,10]. Throughout this progress, interlayer materials have been crucial to support performance enhancements, allowing fine tuning of the limited range of anode and cathode materials to the properties of the active layers. Key developments have included the development of polyethylenedioxythiophene (PEDOT:PSS)[11,12], dipolar and ionic polymers and molecules including self-assembled monolayers[13–19], and inorganic compounds including thiocyanates[20–23].

The current paper focuses on consideration of the high-nuclear polyoxomolybdate cluster compound $(NH_4)_{42}[Mo^{VI}_{72}Mo^{V}_{60}O_{372}(CH_3COO)_{30}(H_2O)_{72}]$ (hereafter referred to as {Mo_{132}}) and derivatives as effective interlayer materials for organic optoelectronic devices. These compounds were first reported by the Müller group and represent an important class of Keplerate-type polyoxometalates (POMs)[24–26]. {Mo_{132}} has a hollow spherical architecture with five-fold symmetry and a diameter of ~ 3.0 nm. It carries 42 negative charges on its outer surface and can be regarded as a fullerene analog. Previous reports for {Mo_{132}} and derivatives mainly

[1]State Key Laboratory of Supramolecular Structure and Materials, College of Chemistry, Jilin University, Changchun, China. [2]Oxford Suzhou Centre for Advanced Research, University of Oxford, Suzhou, China. [3]NEOM Education, Research, and Innovation Foundation, Neom Community 1, Building 4758, Al Khuraybah, Tabuk, Al-Madinah Al-Munawwarah Province, Saudi Arabia. ✉e-mail: jingsong.huang@oxford-oscar.cn; wulx@jlu.edu.cn; fhli@jlu.edu.cn

Scheme 1 | Synthetic process of $\{Mo_{132}\}$-TOA.

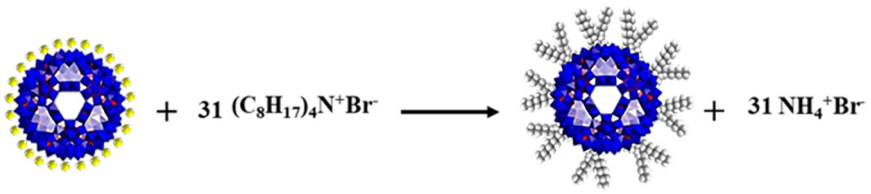

$\{Mo_{132}\}$: $(NH_4)_{42}[Mo^{VI}_{72}Mo^{V}_{60}O_{372}(CH_3COO)_{30}(H_2O)_{72}]$

$\{Mo_{132}\}$-TOA: $((C_8H_{17})_4N)_{31}(NH_4)_{11}[Mo^{VI}_{72}Mo^{V}_{60}O_{372}(CH_3COO)_{30}(H_2O)_{72}]$

focused on structure and basic catalytic properties[27–29]. Recent interest has extended into utilization within dye-sensitized solar cells[30], lithium-ion batteries[31], supercapacitors[32], and perovskite-based photodetectors[33], due to $\{Mo_{132}\}$'s unique redox, ion-trapping, and photoelectric properties[26,34]. This has helped to shed light on the wider application potential of $\{Mo_{132}\}$ and its derivatives for electronic devices. The giant POMs are emerging as attractive components for the design of advanced functional materials and devices[35–38], but to fabricate POM-based devices, it is necessary to deposit high quality thin film coatings. Although $\{Mo_{132}\}$ is usually obtained as an ammonium salt, its derivatization in the form of organic-inorganic ionic hybrids often simplifies integration into functional films, e.g., as a surfactant-encapsulated $\{Mo_{132}\}$ (SEMo)[39]. The resulting hydrophobic surface of SEMo improves solubility in non-aqueous solvents, protects the macroion core, and extends $\{Mo_{132}\}$ use to different environments. Because counter cations can also modulate POM structure and function, as well as controlling solubility[40], the substitution of counter cations with long-chain alkylammonium allows more functional performance[41]. To date, however, $\{Mo_{132}\}$ and SEMo have been little used for organic optoelectronic device applications. An important advance in this regard is to fabricate thin films of $\{Mo_{132}\}$ and SEMo by solution-processing methods e.g., spin-coating or printing[42–47]. The hydrophobic encapsulation *via* electrostatic interaction allows SEMo to be soluble in organic solvents and show poor crystallization behavior, preserving the desired as-deposited isotropic film structure. It is anticipated, further, that different SEMo arrangements can allow for different interfacial dipoles compared to bare $\{Mo_{132}\}$ and potentially qualitatively different effects on substrate work function (WF).

This remains a topic to be more clearly elucidated, motivating the systematic investigation reported in the current paper of the interfacial characteristics for $\{Mo_{132}\}$ thin films and SEMo e.g., $\{Mo_{132}\}$-TOA (see molecular formula in Scheme 1) thin films on a variety of metal and metal oxide electrodes, and their utilization within organic optoelectronic devices. Interface energetics of $\{Mo_{132}\}$ thin films and $\{Mo_{132}\}$-TOA thin films on Al, Ag and ITO are described and application to organic solar cells (OSCs) and polymer light-emitting diodes (PLEDs) is demonstrated. $\{Mo_{132}\}$ and $\{Mo_{132}\}$-TOA thin films can, respectively, upshift and downshift WF via surface interface dipoles. $\{Mo_{132}\}$-TOA as a cathode interlayer (CIL) yields a power conversion efficiency (PCE) of 18% for PM6:L8-BO based OSCs and a current efficiency of 15.24 cd/A for Super Yellow emission-layer based PLEDs. In addition, when $\{Mo_{132}\}$ as anode interlayer (AIL) and $\{Mo_{132}\}$-TOA as CIL are utilized simultaneously, the PCE of OSCs based on PM6:2,2'-((2Z,2'Z)-((12,13-bis(2-ethylhexyl)-3,9-diundecyl-12,13-dihydro-[1,2,5]thiadiazolo[3,4-e]thieno[2",3":4',5']thieno[2',3':4,5]pyrrolo[3,2-g]thieno[2',3':4,5]thieno[3,2-b]indole-2,10-diyl)bis(methanylylidene))bis(5,6-difluoro-3-oxo-2,3-dihydro-1H-indene-2,1-diylidene))dimalononitrile (Y6) surpassed 15%. The same combination of interlayers also yielded 14.95 cd/A current efficiency and 13.08 lm/W power efficiency for Super Yellow emission layer PLEDs. Furthermore, both OSCs and PLEDs with $\{Mo_{132}\}$ and $\{Mo_{132}\}$-TOA displayed better stability. $\{Mo_{132}\}$ is thereby shown to serve as an effective bifunctional interlayer material to optimize organic optoelectronic device performance, enhancing power conversion and light emission efficiencies and increasing lifetime.

Results

Interface energetics of $\{Mo_{132}\}$ and $\{Mo_{132}\}$-TOA thin films on different surfaces

UPS is a powerful tool to characterize interfacial energetics, and gives direct measurements of the WF and ionization potential (IP) of the solids. The WF, corresponding to the difference between Fermi and vacuum levels, is determined from the secondary electron cutoff in the UPS spectra[48]. The magnitude of WF modification depends on the electron transfer strength across the electrode interface and density of states of interfacial materials[49–52]. The IP, corresponding to the difference between valence band and vacuum levels, is determined from the onset of valence band in the UPS spectra and the WF. The electron affinity (EA), corresponding to the difference between conduction band and vacuum levels, is determined from the IP and band gap (E_g) obtained from ultraviolet-visible absorption spectra. The IP of $\{Mo_{132}\}$ is 6.14 eV from UPS measurements in Fig. S6. The EA of $\{Mo_{132}\}$ is 4.39 eV from IP of 6.14 eV and E_g of 1.75 eV from UV-Vis. absorption in Figure S3. In the same way, the IP and EA of $\{Mo_{132}\}$-TOA are 5.48 eV and 3.76 eV, respectively. The interface energetics of ~ 3–4 nm $\{Mo_{132}\}$ and ~ 5–6 nm $\{Mo_{132}\}$-TOA thin films deposited on Al, Ag and ITO have been investigated using UPS (Fig. 1). These films possess approximately monolayer thicknesses of $\{Mo_{132}\}$ and $\{Mo_{132}\}$-TOA[24]. Fig. 1a_1 presents the secondary electron cutoff region (SECR) in the UPS spectra of bare Al, and Al covered by $\{Mo_{132}\}$ (Al /$\{Mo_{132}\}$) and $\{Mo_{132}\}$-TOA (Al/$\{Mo_{132}\}$-TOA) thin films. Fig. 1b_1 presents the SECR in the UPS spectra of bare Ag, and Ag covered by $\{Mo_{132}\}$ (Ag/$\{Mo_{132}\}$) and $\{Mo_{132}\}$-TOA (Ag/$\{Mo_{132}\}$-TOA) thin films. Fig. 1c_1 presents the SECR in the UPS spectra of bare ITO, and ITO covered by $\{Mo_{132}\}$ (ITO/$\{Mo_{132}\}$) and $\{Mo_{132}\}$-TOA (ITO/$\{Mo_{132}\}$-TOA) thin films. The UPS-derived energy level alignment diagrams for the Al/$\{Mo_{132}\}$, Ag/$\{Mo_{132}\}$ and ITO/$\{Mo_{132}\}$ interfaces are depicted in Fig. 1d_2, Fig. 1b_2 and Fig. 1c_2, respectively. The corresponding energy level alignment diagrams for the Al/$\{Mo_{132}\}$-TOA, Ag/$\{Mo_{132}\}$-TOA and ITO/$\{Mo_{132}\}$-TOA interfaces are depicted in Fig. 1a_3, Fig. 1b_3 and c_3, respectively. Intriguingly, we found that the WFs of all the substrates were upshifted when a $\{Mo_{132}\}$ monolayer was deposited due to the formation of a positive interface dipole (Δ) where the positive pole points toward, while the negative pole faces away from, the substrate[53,54], resulting from the feature of $\{Mo_{132}\}$ as an electron acceptor (EA = 4.39 eV). The WF of the Al substrate increased from 3.90 to 4.41 eV, with Δ = 0.51 eV (Fig. 1a_2). The WF of the Ag substrate increased from 4.60 to 5.15 eV, with Δ = 0.55 eV (Fig. 1b_2). Importantly the WF of the ITO substrate increased from 4.67 to 5.16 eV, with Δ = 0.49 eV (Fig. 1c_2). This confirms that $\{Mo_{132}\}$ should be an effective AIL material that can increase the WF of the conventional ITO anode used for organic optoelectronic devices. Conversely, the WFs of all the substrates were downshifted when a $\{Mo_{132}\}$-TOA monolayer was deposited, due to formation of a negative interface dipole (-Δ) with the negative pole pointing towards, and the positive pole away from, the substrate[55],

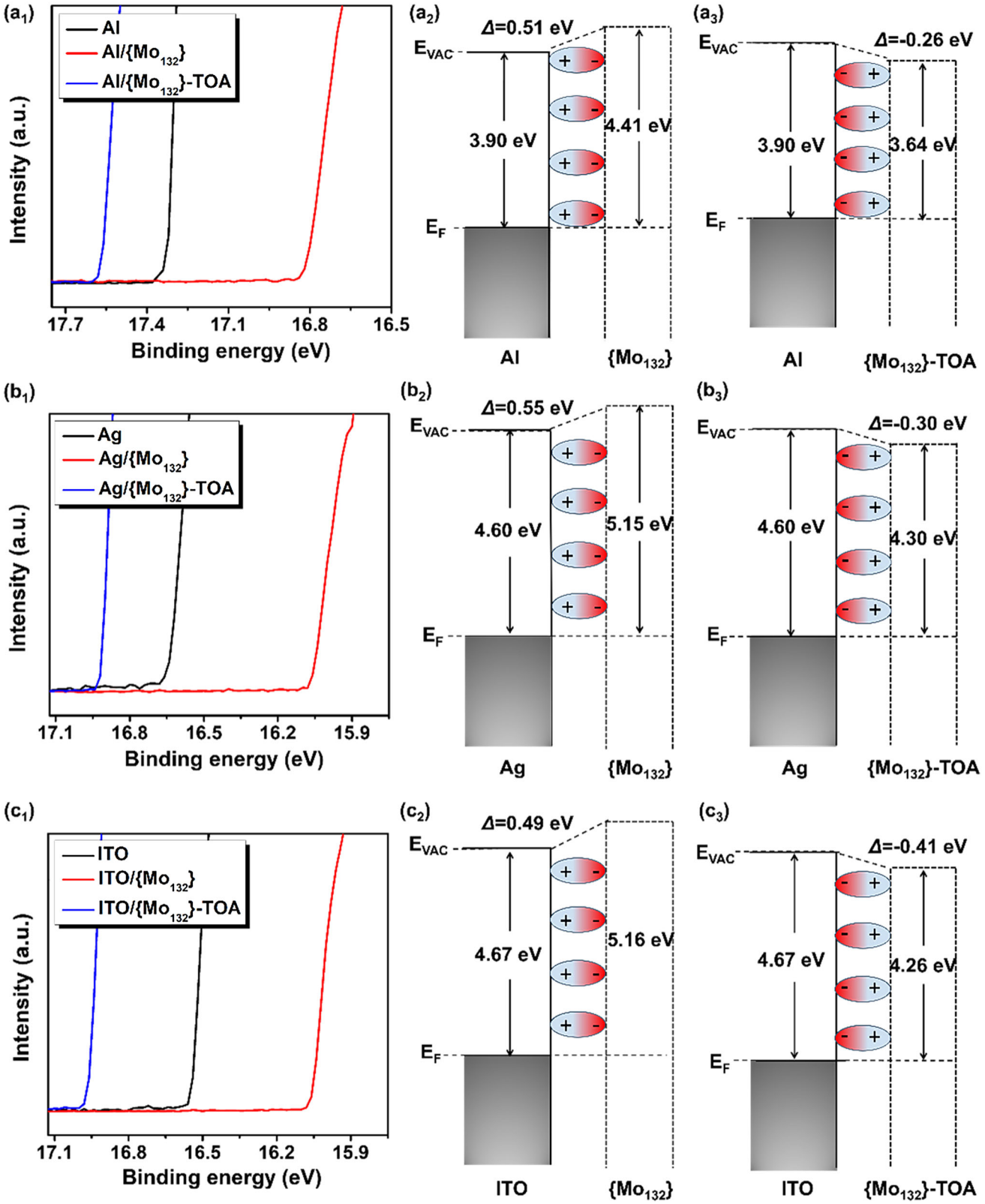

Fig. 1 | UPS spectra and energy level diagrams of $\{Mo_{132}\}$ and $\{Mo_{132}\}$-TOA thin films on different substrates. UPS spectra of $\{Mo_{132}\}$ and $\{Mo_{132}\}$-TOA thin films on Al (**a**$_1$), Ag (**b**$_1$) and ITO (**c**$_1$). Energy level diagrams of $\{Mo_{132}\}$ on Al (**a**$_2$), Ag (**b**$_2$) and ITO (**c**$_2$). Energy level diagrams of $\{Mo_{132}\}$-TOA on Al (**a**$_3$), Ag (**b**$_3$) and ITO (**c**$_3$).

resulting from charge redistribution induced by dipole orientation of $\{Mo_{132}\}^{42-}$ anions and TOA^+ cations in the vicinity of the substrate[56]. The WF of the Al substrate decreased from 3.90 to 3.64 eV, with Δ = -0.26 eV (Fig. 1a$_3$). The WF of the Ag substrate decreased from 4.60 to 4.30 eV, with Δ = -0.30 eV (Fig. 1b$_3$). The WF of the ITO substrate decreased from 4.67 to 4.26 eV, with Δ = -0.41 eV (Fig. 1c$_3$). This confirms that $\{Mo_{132}\}$-TOA should be an effective CIL material that can decrease the WF of metal cathodes used for organic optoelectronic devices.

We consider that this behavior will be equally true for other POMs. Namely, surfactant-encapsulated POM complexes form different interfacial

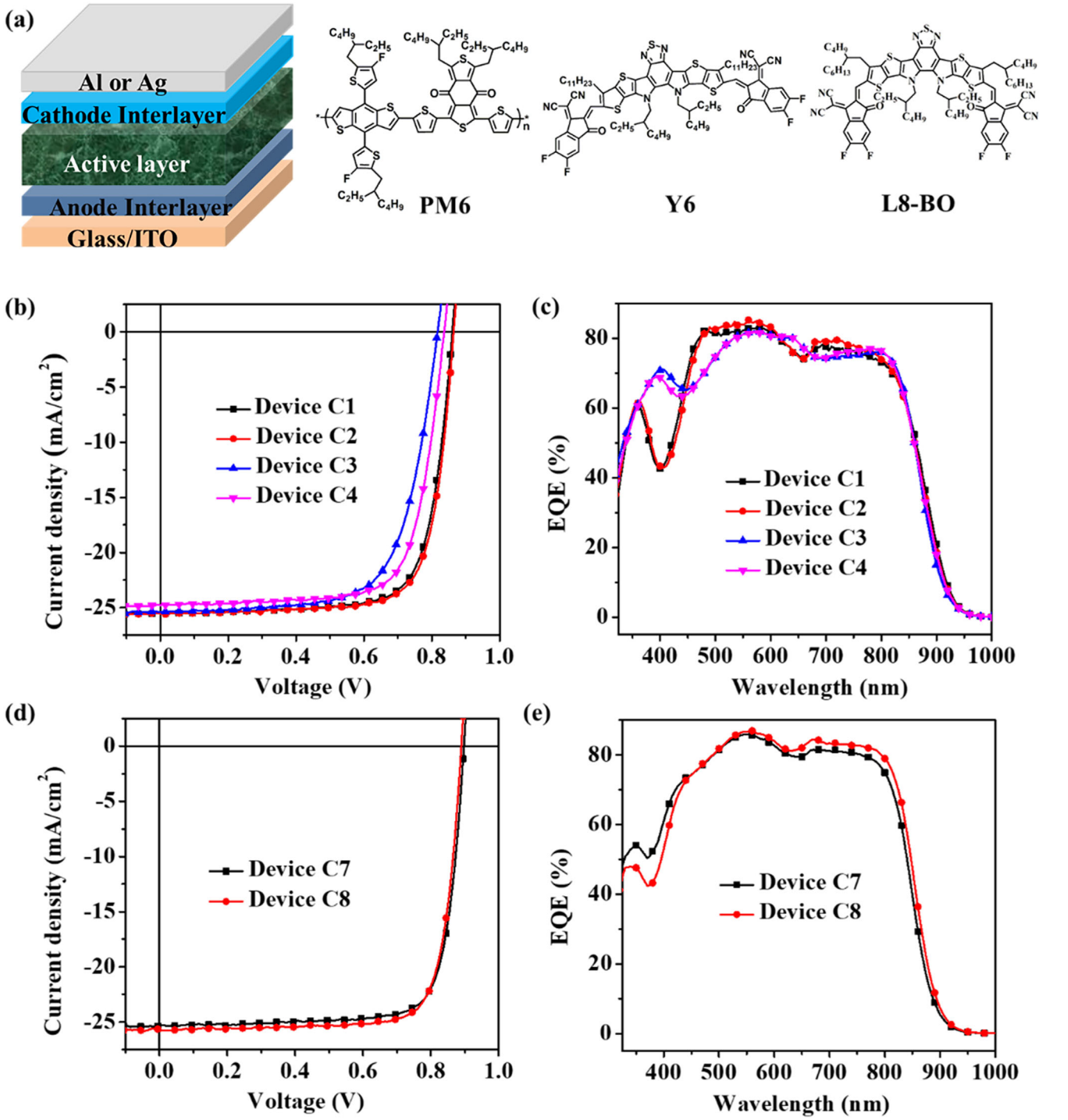

Fig. 2 | Device structure and photovoltaic properties of the OSCs with different cathode and anode interlayers. a Schematic OSC device structure together with molecular structures of PM6, Y6, and Y8-BO. **b** *J-V* characteristics and **c** EQE spectra of PM6:Y6 based OSCs with different cathode and anode interlayers (Table 2). **d** *J-V* characteristics and **e** EQE spectra of PM6:L8-BO based OSCs with Al and Ag cathodes modified by {Mo_{132}}-TOA, respectively (Table 2).

dipoles from un-encapsulated POM films, ultimately resulting in the ability to access both positive and negative WF shifts.

OSC with {Mo_{132}} and {Mo_{132}}-TOA films as electrode interlayers

To evaluate the suitability of {Mo_{132}} and {Mo_{132}}-TOA thin films as anode (AIL) and cathode (CIL) interlayers, respectively, conventional OSCs were fabricated with configuration ITO/AIL/PM6:Y6 or L8-BO/CIL/Al or Ag (Fig. 2). Device type C1 (Table 2) was fabricated as a control device with widely used interlayers PEDOT:PSS (AIL) and PFN-Br (CIL) and an Al cathode. Device type C2 substituted the PFN-Br CIL with {Mo_{132}}-TOA. Device type C3 replaced the PEDOT-PSS AIL with {Mo_{132}}, keeping PFN-Br as CIL. Finally, device type C4 additionally replaced the PFN-Br CIL with {Mo_{132}}-TOA. *J-V* characteristics for these four device types were measured under AM 1.5 G illumination and the *J-V* curves corresponding to the maximum PCEs are shown in Fig. 2b.

Table 1 lists the deduced photovoltaic parameters, including open circuit voltage (V_{OC}), short circuit current (J_{SC}), fill factor (FF) and PCE. At least 20 pixels (size = 2 × 2 mm^2) were measured for each device type and the

Table 1 | Performance values for OSCs with PM6:Y6 and PM6:L8-BO active layers, for different cathode and anode interlayers and cathode metals (Table 2)

Device	V_{OC} (V)	J_{SC} (mA/cm^2)	$J_{SC\text{-}EQE}$ (mA/cm^2)	FF (%)	PCE (%)		R_s (Ω cm^2)	R_{sh} (Ω cm^2)
					Max.	Aver.		
C1[a]	0.860	25.54	24.28	74.9	16.45	16.03	2.65	2412
C2[a]	0.860	25.55	24.38	76.1	16.71	16.34	2.25	5075
C3[a]	0.815	25.39	24.13	68.7	14.21	14.10	4.12	816
C4[a]	0.815	25.12	24.07	73.3	15.01	14.75	3.99	1843
C5[a]	0.850	25.88	24.79	75.2	16.55	16.32	2.41	2857
C6[a]	0.810	25.78	24.50	71.0	14.82	14.50	3.93	952
C7[b]	0.895	25.32	24.13	79.0	17.91	17.53	2.04	1588
C8[b]	0.885	25.70	24.73	79.6	18.11	17.67	2.07	1186

ITO is used in all cases as the transparent anode.
[a] Active layer is PM6:Y6.
[b] Active layer is PM6:L8-BO.

characteristics showed excellent reproducibility. Figure 2c shows the EQE spectra from 325 to 1000 nm. Integrated J_{SC} values ($J_{SC\text{-}EQE}$) were calculated from the EQE spectra (Table 1), and they match well with the J_{SC} values directly obtained from the *J-V* characteristics, within < 5% error. This shows internal consistency and gives confidence that the PCE values shown in Table 1 are not overestimated.

Considering device types C1 and C2, with PEDOT:PSS as AIL we find that using PFN-Br as CIL yields PCE = 16.45% with V_{OC} = 0.86 V, J_{SC} = 25.54 mA/cm^2 and FF = 74.9%. Substituting {Mo_{132}}-TOA as CIL yielded a higher PCE = 16.71%, among the best PCE values reported for OSCs based on PM6:Y6[55], resulting from a higher FF = 76.1%.

To investigate the reason for the improvement in FF of C2 compared to C1, we measured the *J-V* curves of C1 and C2 under dark conditions (Fig. S6a) and plotted the photocurrent density versus effective voltage (J_{ph}-V_{eff}) curves (Fig. S6b). The photocurrent density saturates ($J = J_{ph,sat}$) when V_{eff} approaches 2 V. Under short-circuit conditions, $J_{ph,sc}/J_{ph,sat}$ reflects the exciton dissociation efficiency in the device, while under maximum power conditions, $J_{ph,max}/J_{ph,sat}$ reflects the charge carrier extraction efficiency.

The $J_{ph,sc}/J_{ph,sat}$ values for both devices C1 and C2 are 98.2%, indicating that the exciton dissociation efficiencies are similar when using PFN-Br and {Mo_{132}}-TOA as CIL. Under maximum power output, the $J_{ph,max}/J_{ph,sat}$ values for devices C1 and C2 are 84.7% and 85.5%, respectively, indicating that the charge collection capability of C2 with {Mo_{132}}-TOA as CIL is somewhat superior to that of C1 with PFN-Br.

Space charge limited current (SCLC) measurements were also performed on single electron devices with structure ITO/ZnO/PM6:Y6/CIL/Al.

Fitting to the Mott—Gurney law: $J = \frac{9}{8}\varepsilon_0\varepsilon_r\mu_e\frac{V^2}{L^3}$, where J is the current density, V is the applied bias, L is the thickness of the active layer,ε_0 is the vacuum dielectric constant, andε_r the relative dielectric constant of PM6: Y6 (ε_r = 2.45) should allow determination of the μ_e value for PM6:Y6. As shown in Fig. S6c, the μ_e values measured for the devices with PFN-Br and {Mo_{132}}-TOA are different, namely 3.20×10^{-4} and 4.86×10^{-4} cm^2 V^{-1} s^{-1}, respectively, pointing to different trapping contributions. The trap-filled-limit is reached at V_{TFL} = 0.127 and 0.113 V for the PFN-Br and {Mo_{132}}-TOA devices, respectively (Fig. S6d). The associated trap density, N_t, is calculated from V_{TFL}, according to: $N_t = \frac{2\varepsilon_r\varepsilon_0}{qL^2}V_{TFL}$, where q is the elementary charge. For the single-carrier electron device with PFN-Br as CIL, $N_t = 3.44\times10^{15}$ cm^{-3}, while for the device with {Mo_{132}}-TOA as CIL it is lowered to $N_t = 3.06\times10^{15}$ cm^{-3}. Higher charge collection capability, larger charge carrier mobility, and lower defect state density values facilitate charge carrier transport and reduce charge recombination, thereby improving the FF of device type C2 relative to C1. The series resistance (R_s) and shunt resistance (R_{sh}) values were also calculated from Fig. 2b. Device type C2 had R_s = 2.25 Ω cm^2 and R_{sh} = 5075 Ω cm^2, while device type C1 had R_s = 2.65 Ω cm^2 and R_{sh} = 2412 Ω cm^2. The higher R_{sh} leading to smaller leakage current also rationalizes the higher FF for device type C2.

Device types C3 and C4 both use {Mo_{132}} instead of PEDOT:PSS as AIL, with PFN-Br and {Mo_{132}}-TOA, respectively, as CILs. From Fig. 2b it is seen that whilst {Mo_{132}} worked well as an AIL, the PCEs were slightly lower than for the PEDOT:PSS AIL devices. The PCE of device type C4 reached 15.01%, with V_{OC} = 0.815 V, J_{SC} = 25.12 mA/cm^2 and FF = 73.3%. The PCE for device type C3 was 14.21%, with V_{OC} = 0.815 V, J_{SC} = 25.39 mA/cm^2, and FF = 68.7%.

The slightly lower V_{OC} and FF for device types C3 and C4, relative to C1 and C2 may be due to a poorer contact at the ITO/{Mo_{132}} interface than the ITO/PEDOT:PSS interface. The few-nanometer thickness {Mo_{132}} AIL does not readily cover the entirety of the ITO surface whereas 30–40 nm of PEDOT:PSS readily does. Consequently, it is expected that there will be significantly more surface defects for ITO/{Mo_{132}} than for ITO/PEDOT:PSS. This would lead to increased defect-induced non-radiative recombination in {Mo_{132}}-based devices and consequently reduce their V_{OC} and FF values[57].

The R_s and R_{sh} values for device type C4 are 3.99 Ω cm^2 and 1843 Ω cm^2, respectively, and for C3 4.12 Ω cm^2 and 816 Ω cm^2, respectively. Device type C4 has a higher R_{sh}, which rationalizes the higher FF than for device type C3. It appears that {Mo_{132}}-TOA gives rise to a better interfacial contact with Al than PFN-Br does. To further investigate the contact properties for {Mo_{132}}-TOA and PFN-Br with the Al cathode, we employed UPS to characterize the energy level alignment at the Al/Y6, Al/{Mo_{132}}-TOA/Y6, and Al/PFN-Br/Y6 interfaces, and calculated the electron extraction barrier (EEB). Figure S7 displays the UPS spectra and band bending for Y6/Al without a CIL and with different CILs. The EEB from Y6 to the Al electrode without a CIL was found to be 0.14 eV. When a CIL was introduced the EEB decreased significantly. Specifically, PFN-Br reduced the EEB to 0.08 eV, while the introduction of {Mo_{132}}-TOA resulted in an EEB of only 0.02 eV. These results confirm the better interfacial contact with Al for {Mo_{132}}-TOA than PFN-Br. In addition, higher R_s and lower R_{sh} for the devices with {Mo_{132}} as AIL than found for PEDOT:PSS seem to result from a relatively poor film quality for {Mo_{132}} thin films on ITO. This in turn leads to lower PCEs.

Devices with Ag as the cathode metal were also studied, namely types C5 and C6 (Table 2), both with the same {Mo_{132}}-TOA CIL but different AILs; PEDOT:PSS for C5 and {Mo_{132}} for C6. The resulting *J-V* curves and EQE spectra are shown in Fig. S8, with the extracted parameters listed in Table 1. Maximum PCE values are 16.55% and 14.82% for C5 and C6 devices, respectively. The R_s and R_{sh} values are 2.41 and 2857 Ω cm^2 for C5 and 3.93 and 952 Ω cm^2 for C6 devices. It appears that {Mo_{132}}-TOA makes good contact with Ag too.

Table 2 | Fabricated device structures: Device number; Type; Anode material; Anode Interlayer (AIL) material; Active Layer material; Cathode Interlayer (CIL) material; Cathode material

Device Number	Device Type	Anode	AIL	Active Layer	CIL	Cathode
C1	OSC	ITO	PEDOT:PSS	PM6:Y6	PFN-Br	Al
C2	OSC	ITO	PEDOT:PSS	PM6:Y6	$\{Mo_{132}\}$-TOA	Al
C3	OSC	ITO	$\{Mo_{132}\}$	PM6:Y6	PFN-Br	Al
C4	OSC	ITO	$\{Mo_{132}\}$	PM6:Y6	$\{Mo_{132}\}$-TOA	Al
C5	OSC	ITO	PEDOT:PSS	PM6:Y6	$\{Mo_{132}\}$-TOA	Ag
C6	OSC	ITO	$\{Mo_{132}\}$	PM6:Y6	$\{Mo_{132}\}$-TOA	Ag
C7	OSC	ITO	PEDOT:PSS	PM6:L8BO	$\{Mo_{132}\}$-TOA	Al
C8	OSC	ITO	PEDOT:PSS	PM6:L8BO	$\{Mo_{132}\}$-TOA	Ag
D1	PLED	ITO	PEDOT:PSS	Super Yellow	PFN-Br	Al
D2	PLED	ITO	PEDOT:PSS	Super Yellow	$\{Mo_{132}\}$-TOA	Al
D3	PLED	ITO	$\{Mo_{132}\}$	Super Yellow	PFN-Br	Al
D4	PLED	ITO	$\{Mo_{132}\}$	Super Yellow	$\{Mo_{132}\}$-TOA	Al

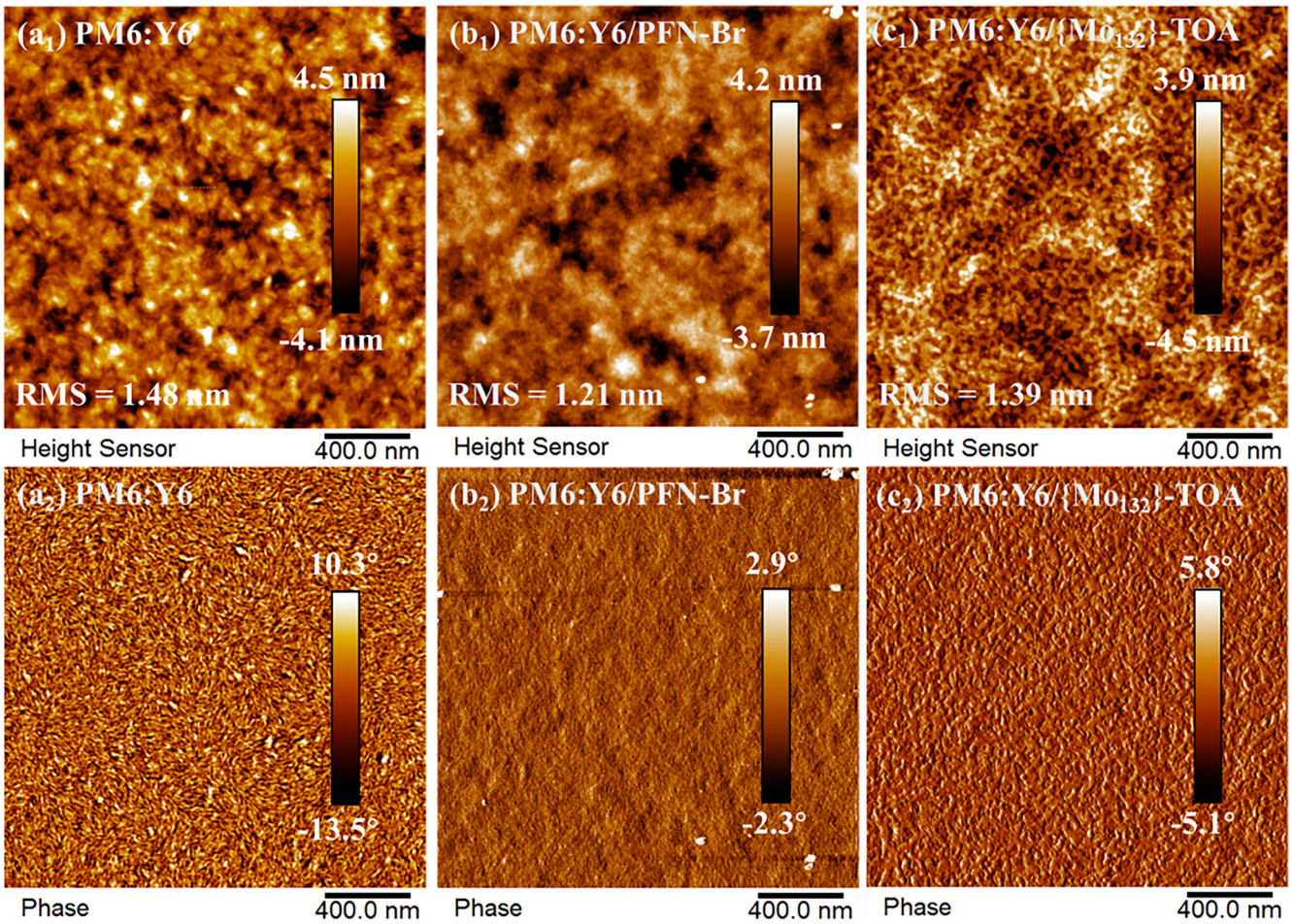

Fig. 3 | AFM Height Images and Phase Images of Bare PM6:Y6 and PM6:Y6 Covered by Different Cathode Interlayers. AFM height images and phase images of PM6:Y6 film ($\mathbf{a_1}$ and $\mathbf{a_2}$), PM6:Y6/PFN-Br film ($\mathbf{b_1}$ and $\mathbf{b_2}$) and PM6:Y6/$\{Mo_{132}\}$-TOA film ($\mathbf{c_1}$ and $\mathbf{c_2}$).

To further demonstrate the versatility of $\{Mo_{132}\}$-TOA as a CIL, the OSC active layer was changed to PM6:L8-BO for device types C7 and C8 (Table 2) with the same PEDOT:PSS AIL for both, but Al and Ag cathodes, respectively. The resulting *J-V* curves and EQE spectra are presented in Figs. 2d, e with the corresponding parameters listed in Table 1. PCE values of 17.91 and 18.11% were obtained for C7 and C8 devices, respectively, close to the PCE = 18.3% reported by Sun et al. for the PM6:L8-BO based OSCs with poly[(9,9-bis(3′-((N,N-dimethyl)-N-ethylammonium)propyl)-2,7-fluorene)-alt-5,5′-bis(2,2′-thiophene)-2,6-naphthalene-1,4,5,8-tetracaboxylic-N,N′-di(2-ethylhexyl)imide]dibromide (PNDIT-F3N-Br) as a CIL[58]. Thereby confirming the promising potential of $\{Mo_{132}\}$-TOA as a CIL material for high efficiency OSCs.

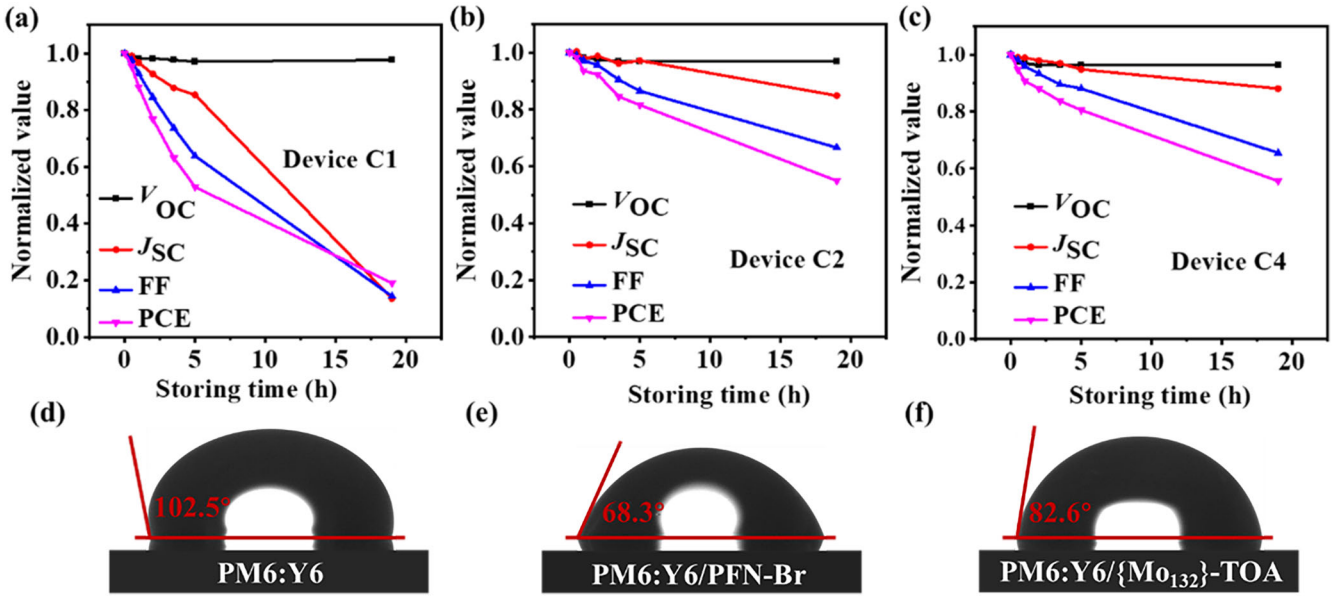

Fig. 4 | Air stability of different unencapsulated devices and water contact angles of bare PM6:Y6 and PM6:Y6 covered by different cathode interlayers. Normalized V_{OC}, J_{SC}, FF and PCE for unencapsulated device types C1 (**a**), C2 (**b**) and C4 (**c**) *versus* storage time in air. Photos of water droplets on the surface of **d** PM6:Y6, **e** PM6:Y6/PFN-Br and **f** PM6:Y6/{Mo_{132}}-TOA films.

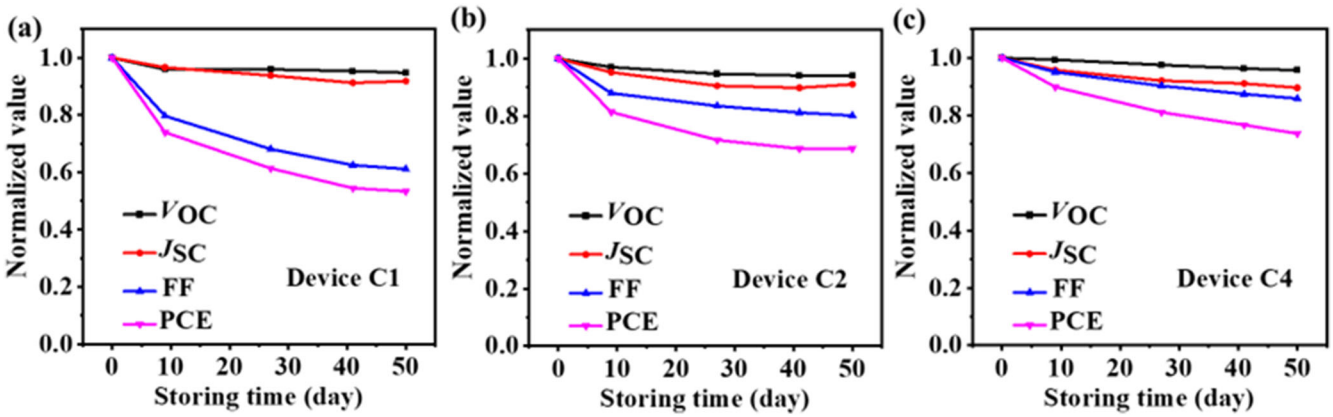

Fig. 5 | Light stability of different encapsulated devices. Normalized V_{OC}, J_{SC}, FF and PCE of encapsulated device types C1 (**a**), C2 (**b**), and C4 (**c**) *versus* storage time under constant 10000 lux LED soaking.

To further investigate the interface formed between ITO and the {Mo_{132}} AIL and between the active layer and {Mo_{132}}-TOA CIL, we have used atomic force microscopy (AFM) to measure the surface morphology. Fig. 3 shows AFM height and phase images of films of PM6:Y6 (a_1 and a_2), PM6:Y6 covered by PFN-Br (b_1 and b_2) and PM6:Y6 covered by {Mo_{132}}-TOA (c_1 and c_2). The root-mean-squared (RMS) surface roughness values for PM6:Y6, PM6:Y6/PFN-Br and PM6:Y6/{Mo_{132}}-TOA are 1.48 nm, 1.21 nm and 1.39 nm, respectively. Both PFN-Br and {Mo_{132}}-TOA have little effect on the RMS roughness of the PM6:Y6 film. Different from PFN-Br, however, the {Mo_{132}}-TOA on PM6:Y6 shows a granular morphology with apparent boundaries and is homogenous, closely packed and well-distributed (Fig. 3c_1 and c_2). In addition, AFM height images and phase images for ITO, and ITO covered by PEDOT:PSS and {Mo_{132}} AILs were also recorded and are shown in Figure S9. PEDOT:PSS and {Mo_{132}} both reduced the RMS roughness for bare ITO from 4.28 nm to 1.38 nm, and 2.23 nm, respectively. It should be noted, however, that the few-nanometer thickness {Mo_{132}} AIL did not completely cover the ITO surface whereas the 30-40 nm PEDOT:PSS AIL did, resulting in a higher roughness for ITO/{Mo_{132}} compared to ITO/PEDOT:PSS. As a result, the V_{OC} and FF of the devices with PEDOT:PSS (C1 and C2) are notably higher than for otherwise equivalent devices with {Mo_{132}} (C3 and C4).

Stability within devices is an important consideration for OSC materials to be commercially viable. Unencapsulated device stability in air (temperature: 20 °C–25 °C, humidity: 30–40%) and light stability for encapsulated devices have, consequently, been investigated. Fig. 4 shows normalized V_{OC}, J_{SC}, FF and PCE values for unencapsulated device types C1 (Fig. 4a), C2 (Fig. 4b) and C4 (Fig. 4c) as a function of storage time in air. The symbols show the times at which measurements were taken and the connecting lines provide a guide to the eye. Device types C2 and C4 with a {Mo_{132}}-TOA CIL exhibit better device stability than device type C1 with PFN-Br. Smaller reductions in J_{SC} and FF lead to smaller reductions in PCE. In particular, device type C4 with {Mo_{132}} as AIL exhibits a smaller reduction in J_{SC} than C2 with PEDOT:PSS as AIL, potentially due to the acidity of PEDOT:PSS[59].

To seek clarity on why the devices with a {Mo_{132}}-TOA CIL have better in-air stability than devices with PFN-Br, water surface-wetting characteristics of PM6:Y6, PM6:Y6/PFN-Br and PM6:Y6/{Mo_{132}}-TOA films were investigated. Water contact angles were measured for PM6:Y6, PM6:Y6/PFN-Br, and PM6:Y6/{Mo_{132}}-TOA surfaces (Fig. 4d–f) yielding 102.5°,

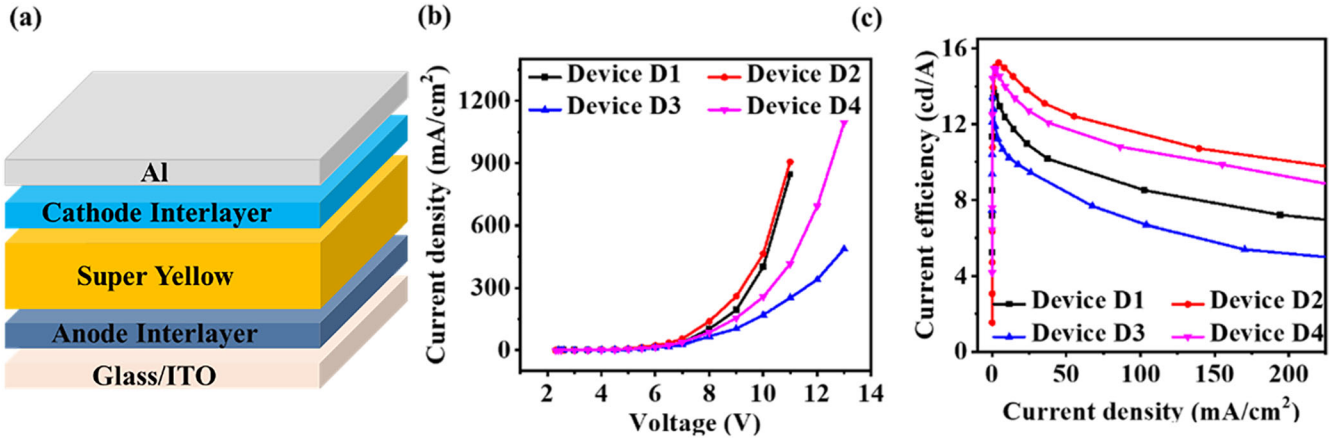

Fig. 6 | Device structure and photoelectrical properties of the PLEDs with different cathode and anode interlayers. a Schematic device structure for Super Yellow PLEDs. **b** Current density-voltage curves and (**c**) current efficiency-current density characteristics for Super Yellow PLEDs with different cathode and anode interlayer materials.

68.3° and 82.6°, respectively. The PM6:Y6/PFN-Br surface is clearly more hydrophilic than the PM6:Y6/{Mo_{132}}-TOA surface, consistent with device type C1 exhibiting poorer stability than device types C2 and C4. Light stability of encapsulated C1, C2 and C4 devices was also tested under constant 10000 lux LED soaking and is shown in Fig. 5. After 50 days, the PCEs of C1, C2 and C4 devices reduced to 8.77%, 11.48%, and 11.05%, namely, to fractions of 53.3%, 68.7% and 73.6% of the originally recorded PCE values, respectively. The stability of C2 and C4 devices with a {Mo_{132}}-TOA CIL is better than for C1 devices with PFN-Br maybe because PFN-Br includes mobile Br^- ions[60]. The stability of C4 devices with {Mo_{132}} is better than C2 with PEDOT:PSS, likely due to the acidity of PEDOT:PSS. Therefore C4 with {Mo_{132}} as AIL and {Mo_{132}}-TOA as CIL showed the best device stability under both storage in-air and encapsulated light soaking tests.

PLEDs with {Mo_{132}} and {Mo_{132}}-TOA films as electrode interlayers

To demonstrate the wider utility of {Mo_{132}} and {Mo_{132}}-TOA films as electrode interlayers for organic optoelectronic devices, we also fabricated PLEDs with structure: ITO/PEDOT:PSS or {Mo_{132}} AIL/Super Yellow emission layer/PFN-Br or {Mo_{132}}-TOA CIL/Al (Table 2 and Fig. 6). Device types with PEDOT:PSS as AIL were fabricated with PFN-Br (D1) and {Mo_{132}}-TOA (D2) as CIL. Devices with {Mo_{132}} as AIL were also fabricated with PFN-Br (D3) and {Mo_{132}}-TOA (D4) CIL layers.

All four device types yielded the same electroluminescence spectrum, characteristic of Super Yellow (Figure S10), demonstrating an absence of exciplex formation. Current density-voltage and current efficiency-current density characteristics for D1-D4 devices are presented in Fig. 6b, c, respectively. Luminance-voltage and power efficiency-current density characteristics are shown in Fig. S11 and extracted performance parameters are listed in Table S2. All four device types exhibited the same turn-on voltage, V_{on} = 2.5 V. D2 yielded a maximum luminance of 43430 cd/m^2 with current efficiency 15.24 cd/A while D1 had a maximum luminance of 35090 cd/m^2 with current efficiency 13.67 cd/A. D4 yielded a maximum luminance of 39030 cd/m^2 with current efficiency 14.95 cd/A while Device D3 had a maximum luminance of 14330 cd/m^2 with current efficiency 13.41 cd/A. The efficiencies of D2 are comparable to those reported in the literature for Super Yellow PLEDs[61,62]. These results indicate that {Mo_{132}} and {Mo_{132}}-TOA can theoretically work as AIL and CIL, respectively, in PLEDs. {Mo_{132}}-TOA as CIL in D2 and D4 resulted in higher current efficiencies than for PFN-Br in D1 and D3. In particular, D4 exhibited the best power efficiency of 13.08 lm/W (Table S2). Moreover, efficiency roll-off in D2 and D4 was lower than in D1 and D3, as shown in Fig. S12, indicating that the devices with {Mo_{132}}-TOA are also more stable.

However, for the {Mo_{132}}-TOA-based PLEDs, achieving a current density of 100 mA/cm^2 requires a voltage exceeding 8 V. This large drive voltage, significantly higher than the reported literature range of 2 - 4 V, is a consequence of the mismatch between the Al/{Mo_{132}}-TOA WF (WF = 3.63 eV) and the EA (EA ~ 3 eV) for Super Yellow. The resulting barrier hinders electron injection into the emission layer. Therefore, the results for {Mo_{132}}-TOA as a CIL in Super Yellow devices indicate only preliminarily potential for use in PLEDs at this point.

Future studies on the use of {Mo_{132}}-TOA as a CIL in PLEDs will focus on emission layers and/or electron transport layers that possess more closely matched EA values. Examples of more suitable emission layer materials would be poly(9,9-dioctylfluorene-*co*-benzothiadiazole) and the related poly(90F8:10BT), a commercially available copolymer comprising 90% dioctylfluorene and 10% benzothiadiazole moities. These widely studied green emission polymers have electron affinities EA ~ 3.5 eV[63,64].

Discussion

{Mo_{132}} and {Mo_{132}}-TOA thin films are able to upshift and downshift the WF values for typical organic optoelectronic device electrodes (Al, Ag and ITO), allowing optimization of both electron and hole injection. {Mo_{132}} produces a positive pole at the electrode surface and acts as an AIL. {Mo_{132}}-TOA produces a negative pole at the electrode surface and acts as a CIL. Using {Mo_{132}}-TOA as CIL yielded PCE values of 16.71% and 18.11% for PM6:Y6 and PM6:L8-BO active layer OSCs, respectively. It also afforded a current efficiency of up to 15.24 cd/A for Super Yellow PLEDs. When {Mo_{132}} is used as AIL and {Mo_{132}}-TOA as CIL, the PCE of OSCs based on a PM6:Y6 active layer reached 15.01% and the current efficiency for the PLEDs reached 14.95 cd/A. Importantly, the OSCs with {Mo_{132}} AIL and {Mo_{132}}-TOA CIL also displayed improved device stability.

Method

Materials

poly[(2,6-(4,8-bis(5-(2-ethylhexyl)-4-fluorothiophen-2-yl)-benzo[1,2-b:4,5-b']dithiophene))-alt-(5,5-(1',3'-di-2-thienyl-5',7'-bis(2-ethylhexyl) benzo[1',2'-c:4',5'-c']dithiophene-4,8-dione))]:2,2'-((2Z,2'Z)-((12,13-bis(2-ethylhexyl)-3,9-(2-butyloctyl)-12,13-dihydro-[1,2,5]thiadiazolo[3,4-e] thieno[2",3":4',5']thieno[2',3':4,5]pyrrolo[3,2-g]thieno[2',3':4,5]thieno[3,2-b]indole-2,10-diyl)bis(methanylylidene))bis(5,6-difluoro-3-oxo-2,3-dihydro-1H-indene-2,1-diylidene))dimalononitrile (PM6) and poly(9,9-bis(3'-(N,N-dimethyl)-N-ethylammoinium-propyl-2,7-fluorene)-alt-2,7-(9,9-dioctylfluorene))dibromide (PFN-Br) were purchased from Solarmer Materials Inc. Y6 and 2,2'-((2Z,2'Z)-((12,13-bis(2-ethylhexyl)-3,9-(2-butyloctyl)-12,13-dihydro-[1,2,5]thiadiazolo[3,4-e]thieno[2",3":4',5'] thieno[2',3':4,5]pyrrolo[3,2-g]thieno[2',3':4,5]thieno[3,2-b]indole-2,10-diyl)

bis(methanylylidene))bis(5,6-difluoro-3-oxo-2,3-dihydro-1H-indene-2,1-diylidene))dimalononitrile (L8-BO) were provided by Hyper, Inc. Super Yellow and polyethylenedioxythiophene:polystyrenesulphonate (PEDOT:PSS Baytron PVP Al 4083) were obtained from Xi'an Polymer Light Technology Corp. and Heraeus Inc., Germany, respectively. Chloroform (CF), toluene, 1-chloronaphthalene (CN) and methanol were supplied by Sigma-Aldrich. Raw materials for preparing $\{Mo_{132}\}$ and $\{Mo_{132}\}$-TOA were obtained from commercial sources. All the materials were used as received.

Preparation of $\{Mo_{132}\}$ and $\{Mo_{132}\}$-TOA

$\{Mo_{132}\}$ was synthesized according to the procedure described in ref. 24. The preparation of $\{Mo_{132}\}$-TOA ($((C_8H_{17})_4N)_{31}(NH_4)_{11}[Mo^{VI}_{72}Mo^{V}_{60}O_{372}(CH_3COO)_{30}(H_2O)_{72}]$) is as following. $\{Mo_{132}\}$ (100 mg) and tetraoctylammonium (TOA) bromide (80 mg) were separately dissolved in 10 mL mixtures of water and ethanol (1:1). The $\{Mo_{132}\}$ solution was slowly dripped into the TOA bromide solution. They reacted at room temperature in a molar ratio of 1:31 and a red-brown precipitate was obtained during the stirring process. The precipitate was filtered after stirring for 24 h, washed with H_2O three times and then dried in vacuo to obtain $\{Mo_{132}\}$-TOA as presented in Scheme 1. Chemical structures were confirmed by elemental analysis, Fourier-transform infrared (FTIR), Raman and Electron paramagnetic resonance (EPR) spectroscopy as shown in Table S1 and Figures. S1–3 in Supporting information. Ultraviolet-visible absorption spectra of $\{Mo_{132}\}$ and $\{Mo_{132}\}$-TOA thin films on ITO were presented in Figure S4. The transmission spectra of ITO, PEDOT:PSS on ITO, and $\{Mo_{132}\}$ on ITO demonstrated that $\{Mo_{132}\}$ exhibit only a minor effect on the transmittance of ITO from 300 to 1000 nm (Figure S5).

Fabrication of OSC and polymer light emitting diodes

The selected OSC structure used in our studies comprised ITO/AIL/active layer/CIL/Al or Ag (see Table 2) and was fabricated as follows:

(i) For conventional devices, thoroughly cleaned ITO substrates were treated with UV ozone for 30 minutes. Then a 30-40 nm PEDOT:PSS AIL was spin-coated on top and annealed at 110 °C for 30 min in an inert atmosphere glove-box. Next 90-100 nm PM6:Y6 (1:1.2 weight ratio, 16 mg/ml in total) was deposited onto the PEDOT:PSS film and baked at 70 °C for 10 min or alternatively PM6:L8-BO (1:1.2 weight ratio, 15.4 mg/ml in total) was deposited onto the PEDOT:PSS film and baked at 80 °C for 10 min. Next 0.5 mg/mL PFN-Br in methanol solution was spin-coated on top of the active layers. Finally, 100 nm Al or Ag was thermally evaporated on top of the CIL under a pressure of 3×10^{-4} Pa. The effective area of each device was 2×2 mm^2.

(ii) For polyoxomolybdate interlayer modified devices, when used for the AIL, 1.25 mg/mL $\{Mo_{132}\}$ in methanol solution was spin-coated directly on the ITO without any UV ozone pre-treatment. After deposition of active photovoltaic layers (PM6:Y6 or PM6:L8-BO) as described above, for devices with a polyoxomolybdate CIL, 0.5 mg/mL $\{Mo_{132}\}$-TOA in methanol solution was spin-coated on top. Finally, as for the conventional device, 100 nm Al or Ag was thermally evaporated through a shadow mask onto the CIL at 3×10^{-4} Pa pressure to again define 2×2 mm^2 device areas.

The selected PLED structure used in our studies comprised ITO/AIL/Emission layer/CIL/Al (see Table 2) and was fabricated as follows:

(i) For conventional devices, thoroughly cleaned ITO substrates were treated with UV ozone for 30 min. Then 30–40 nm PEDOT:PSS was spin-coated on top and annealed at 110 °C for 30 min in a glove-box. Next an 80 nm Super Yellow emission layer was spin-coated onto the PEDOT:PSS film from 6 mg/ml toluene solution and dried *in vacuo* for 30 min. Then a 0.5 mg/mL PFN-Br methanol solution was spin-coated on the Super Yellow film to generate the CIL. Finally, 100 nm Al was thermally evaporated on top at 3×10^{-4} Pa pressure, to yield 2×2 mm^2 active area devices.

(ii) For polyoxomolybdate interlayer modified devices, when used for the AIL, 1.25 mg/mL $\{Mo_{132}\}$ was spin-coated directly onto the cleaned ITO substrates. After deposition of a Super Yellow emission layer (as described above), for devices with a polyoxomolybdate CIL, 0.5 mg/mL$\{Mo_{132}\}$-TOA in methanol solution was spin-coated on top. Finally, 100 nm Al was thermally evaporated at 3×10^{-4} Pa to define device areas of 2×2 mm^2.

Measurements and Characterization

Ultraviolet photoelectron spectroscopy (UPS) was carried out using a monochromated He Iα (21.22 eV) discharge lamp with a VG Scienta (Sweden) R3000 analyzer in ultrahigh vacuum at a pressure of 1×10^{-10} mbar. Current density-voltage (*J-V*) characteristics of the OSCs were measured with an Agilent B1500A Semiconductor Device Analyzer (Keysight Technologies, USA) with an *I-V* module under illumination and in the dark in the glove box. The performance of the OSCs was tested under 100 mW cm^{-2} simulated 1 sun AM 1.5 G full spectrum solar irradiation (Enli Technology Co., Ltd. Taiwan, China, model #SS-F5-3A), with intensity calibration via a standard silicon photodiode traced to the National Institute of Metrology, China. External quantum efficiency (EQE) spectra were recorded with a QTEST HIFINITY 5 (Crowntech Inc., USA) quantum efficiency measurement system at 25 °C in atmosphere. AFM images were obtained using a Dimension Fast Scan AFM (Bruker, USA) in tapping mode. Water contact angles were measured with a DSA-30 drop-shape analysis system (Krüss, Germany) in air. Elemental analysis was carried out with an Elementar (Germany) vario MICRO cube organic analysis system. Fourier transform infrared (FT-IR) spectra were measured using a Bruker (Germany) Vertex 80 V spectrometer. Raman spectra were recorded using a Renishaw (UK) Raman system model 1000 spectrometer with 532 nm laser excitation. Ultraviolet-visible (UV-vis) spectra were recorded with a Shimadzu (Japan) UV-3101 PC spectrometer. Electron Paramagnetic Resonance (EPR) spectra were measured by a Bruker (Germany) ELEXSYS-II E500 CW-EPR spectrometer in air. Electroluminescence (EL) spectra and luminescence were measured with a Horiba (Japan) Spectrascan PR-650 photometer. The Current-voltage characteristics, current efficiency and power efficiency for the PLEDs were measured with a computer-controlled Keithley (UK) 2400 Source Meter under ambient atmosphere. The thickness of thin films was measured via a Bruker (Germany) Dektak 150 surface profilometer.

Data availability

The data that support the findings of this study are available from the corresponding author, upon reasonable request.

Received: 18 June 2025; Accepted: 13 November 2025;
Published online: 24 January 2026

References

1. Burroughes, J. H. et al. Light-emitting diodes based on conjugated polymers. *Nature* **347**, 539–541 (1990).
2. Greenham, N. C. et al. Efficient light-emitting diodes based on polymers with high electron affinities. *Nature* **365**, 628–631 (1993).
3. Friend, R. H. et al. Electroluminescence in conjugated polymers. *Nature* **397**, 121–128 (1999).
4. Marks, R. N. et al. The photovoltaic response in poly(p-phenylene vinylene) thin-film devices. *Condens. Matter* **6**, 1379–1394 (1994).
5. Kim, Y. et al. A strong regioregularity effect in self-organising conjugated polymer films and high efficiency polythiophene:fullerene solar cells. *Nat. Mater.* **5**, 197–203 (2006).
6. Huang, J. et al. High efficiency flexible ITO-free polymer/fullerene photodiodes. *Phys. Chem. Chem. Phys.* **8**, 3904–3908 (2006).
7. Sirringhaus, H. et al. Mobility enhancement in conjugated polymer field-effect transistors through chain alignment in a liquid crystalline phase. *Appl. Phys. Lett.* **77**, 406–408 (2000).
8. Nam, S. et al. Significant performance improvement in n-channel organic field-effect transistors with C_{60}:C_{70} co-crystals induced by poly(2-ethyl-2-oxazoline) nanodots. *Adv. Mater.* **33**, 2100421 (2021).
9. Le Roux, F. et al. Enhanced and polarization-dependent coupling for photoaligned liquid crystalline conjugated polymer microcavities. *ACS Photonics* **7**, 746–758 (2020).

10. Le Roux, F. et al. Efficient anisotropic polariton lasing using molecular conformation and orientation in organic microcavities. *Adv. Funct. Mater.* **32**, 2209241 (2022).
11. Lane, P. A. et al. Elimination of hole injection barriers by conducting polymer anodes in polyfluorene light-emitting diodes. *Phys. Rev. B* **74**, 125320 (2006).
12. Levermore, P. A. et al. Highly conductive poly(3,4-ethylenedioxythiophene) films by vapor phase polymerization and their application in efficient organic light emitting diodes. *Adv. Mater.* **19**, 2379–2385 (2007).
13. Xu, W. et al. Fluorene-based cathode interlayer polymers for high performance solution processed organic optoelectronic devices. *Org. Electron.* **15**, 1244–1253 (2014).
14. Nam, S. et al. Inverted polymer:fullerene solar cells exceeding 10% efficiency with poly(2-ethyl-2-oxazoline) nanodots on electron-collecting buffer layers. *Nat. Commun.* **6**, 8929 (2015).
15. Suh, M. et al. High-efficiency polymer LEDs with fast response time fabricated via selection of electron-injecting conjugated polyelectrolyte backbone structure. *ACS Appl. Mater. Interfaces* **7**, 26566–26571 (2015).
16. Kang, C.-M. et al. 1-GHz pentacene diode rectifiers enabled by controlled film deposition on SAM-treated Au anodes. *Adv. Electron. Mater.* **2**, 1500282 (2016).
17. Nam, S. et al. Polyacetylene-based polyelectrolyte as a universal interfacial layer for efficient inverted polymer solar cells. *Org. Elect.* **48**, 61–67 (2017).
18. Seo, J. et al. Nano-crater morphology in hybrid electron-collecting buffer layers for high efficiency polymer: nonfullerene solar cells with enhanced stability. *Nanoscale Horiz.* **4**, 472–479 (2019).
19. Gedda, M. et al. High-efficiency perovskite-organic blend light-emitting diodes featuring self-assembled monolayers as hole-injecting interlayers. *Adv. Energy Mater.* **13**, 2201396 (2023).
20. Perumal, A. et al. High-efficiency, solution-processed, multilayer phosphorescent organic light emitting diodes with a copper thiocyanate hole injection/transport layer. *Adv. Mater.* **27**, 93–100 (2015).
21. Yaacobi-Gross, N. et al. High efficiency organic photovoltaic cells based on the solution-processable hole transporting interlayer copper thiocyanate (CuSCN) as a replacement for PEDOT: PSS. *Adv. Energy Mater.* **5**, 1401529 (2015).
22. Wang, B. et al. Properties and applications of copper(I) thiocyanate (CuSCN) hole-transport interlayers processed from different solvents. *Adv. Electron. Mater.* **8**, 2101253 (2022).
23. Peng, Y. et al. Efficient organic solar cells using copper(I) iodide (CuI) hole transport layers. *Appl. Phys. Lett.* **106**, 243302 (2015).
24. Müller, A. et al. Organizational forms of matter: an inorganic super fullerene and keplerate based on molybdenum oxide. *Angew. Chem. Int. Ed.* **37**, 3360–3363 (1998).
25. Melgar, D. et al. Electronic structure studies on the whole Keplerate family: predicting new members. *Chem. Eur. J.* **23**, 5338–5344 (2017).
26. Müller, A. et al. From linking of metal-oxide building blocks in a dynamic library to giant clusters with unique properties and towards adaptive chemistry. *Chem. Soc. Rev.* **41**, 7431–7463 (2012).
27. Rezaeifard, A. et al. Catalytic epoxidation activity of keplerate polyoxomolybdate nanoball toward aqueous suspension of olefins under mild aerobic conditions. *J. Am. Chem. Soc.* **135**, 10036–10039 (2013).
28. Kopilevich, S. et al. Catalysis in a porous molecular capsule: activation by regulated access to sixty metal centers spanning a truncated icosahedron. *J. Am. Chem. Soc.* **134**, 13082–13088 (2012).
29. Zhou, Z. et al. Big to small: ultrafine Mo_2C particles derived from giant polyoxomolybdate clusters for hydrogen evolution reaction. *Small* **15**, 1900358 (2019).
30. Xu, S. et al. Keplerate-type polyoxometalate/semiconductor composite electrodes with light-enhanced conductivity towards highly efficient photoelectronic devices. *J. Mater. Chem. A* **4**, 14025–14032 (2016).
31. Liu, W. et al. Investigation of the enhanced lithium battery storage in a polyoxometalate model: from solid spheres to hollow balls. *Small Methods* **2**, 1800154 (2018).
32. Dong, Y. et al. rGO functionalized with a highly electronegative keplerate-type polyoxometalate for high-energy-density aqueous asymmetric supercapacitors. *Chem. Asian J.* **13**, 3304–3313 (2018).
33. Xu, X. et al. The dual effect of "inorganic fullerene" $\{Mo_{132}\}$ doped with SnO_2 for efficient perovskite-based photodetectors. *Mater. Chem. Front.* **5**, 6931–6940 (2021).
34. Li, H. et al. Self-assembly and ion-trapping properties of inorganic nanocapsule-surfactant hybrid spheres. *Soft Matter* **7**, 2668–2673 (2011).
35. Yang, L. et al. The intrinsic charge carrier behaviors and applications of polyoxometalate clusters based materials. *Adv. Mater.* **33**, 2005019 (2021).
36. Cherevan, A. S. et al. Polyoxometalates on functional substrates: concepts, synergies, and future perspectives. *Adv. Sci.* **7**, 1903511 (2020).
37. Gao, Y. et al. Polyoxometalates as chemically and structurally versatile components in self-assembled materials. *Chem. Sci.* **13**, 2510–2527 (2022).
38. Duan, F. et al. Polyoxometalate-based ionic frameworks for highly selective CO_2 capture and separation. *CCS Chem.* **3**, 2676–2687 (2021).
39. Volkmer, D. et al. Toward nanodevices: synthesis and characterization of the nanoporous surfactant-encapsulated Keplerate $(DODA)_{40}(NH_4)_2[(H_2O)_n{\subset}Mo_{132}O_{372}(CH_3COO)_{30}(H_2O)_{72}]$. *J. Am. Chem. Soc.* **122**, 1995–1998 (2000).
40. Wang, G. et al. Nanostructured polymer composite electrolytes with self-assembled polyoxometalate networks for proton conduction. *CCS Chem.* **4**, 151–161 (2022).
41. Kurth, D. G. et al. Biologically inspired polyoxometalate–surfactant composite materials. Investigations on the structures of discrete, surfactant-encapsulated clusters, monolayers, and Langmuir–Blodgett films of $(DODA)_{40}(NH_4)_2[(H_2O)_n{\subset}Mo_{132}O_{372}(CH_3CO_2)_{30}(H_2O)_{72}]$. *J. Chem. Soc. Dalton Trans.* **21**, 3989–3998 (2000).
42. Chen, Y. et al. Insights into the working mechanism of cathode interlayers in polymer solar cells via $[(C_8H_{17})_4N]_4[SiW_{12}O_{40}]$. *J. Mater. Chem. A* **4**, 19189–19196 (2016).
43. Qiu, J. et al. Surfactant-encapsulated polyoxometalate complex as a cathode interlayer for nonfullerene polymer solar cells. *CCS Chem.* **4**, 975–986 (2022).
44. Vasilopoulou, M. et al. Old metal oxide clusters in new applications: spontaneous reduction of Keggin and Dawson polyoxometalate layers by a metallic electrode for improving efficiency in organic optoelectronics. *J. Am. Chem. Soc.* **137**, 6844–6856 (2015).
45. Kang, Q. et al. An inorganic molecule-induced electron transfer complex for highly efficient organic solar cells. *J. Mater. Chem. A* **8**, 5580–5586 (2020).
46. Kang, Q. et al. N-doped inorganic molecular clusters as a new type of hole transport material for efficient organic solar cells. *Joule* **5**, 646–658 (2021).
47. Yang, Y. et al. Inorganic molecular clusters with facile preparation and neutral pH for efficient hole extraction in organic solar cells. *ACS Appl. Mater. Interfaces* **12**, 39462–39470 (2020).
48. Li, F. et al. Tuning work function of noble metals as promising cathodes in organic electronic devices. *Chem. Mater.* **21**, 2798–2802 (2009).
49. Braun, S. et al. Fermi level pinning at interfaces with tetrafluorotetracyanoquinodimethane (F4-TCNQ): the role of integer charge transfer states. *Chem. Phys. Lett.* **438**, 259–262 (2007).
50. Lange, I. et al. Band bending in conjugated polymer layers. *Phys. Rev. Lett.* **106**, 216402 (2011).

51. Khoshkhoo, M. et al. The role of the density of interface states in interfacial energy level alignment of PTCDA. *Org. Electron* **49**, 249–254 (2017).
52. Oehzelt, M. et al. Organic semiconductor density of states controls the energy level alignment at electrode interfaces. *Nat. Commun.* **5**, 4174 (2014).
53. Crispin, X. et al. Characterization of the interface dipole at organic/metal interfaces. *J. Am. Chem. Soc.* **124**, 8131–8141 (2002).
54. Braun, S. et al. Energy-level alignment at organic/metal and organic/organic interfaces. *Adv. Mater.* **21**, 1450–1472 (2009).
55. Yao, J. et al. Cathode engineering with perylene-diimide interlayer enabling over 17% efficiency single-junction organic solar cells. *Nat. Commun.* **11**, 2726 (2020).
56. Yao, L. et al. Conjugated polymer zwitterions: efficient interlayer materials in organic electronics. *Acc. Chem. Res.* **49**, 2478–2488 (2016).
57. Yali, C. et al. Mitigating V_{OC} loss in tin perovskite solar cells via simultaneous suppression of bulk and interface nonradiative recombination. *ACS Appl. Mater. Interfaces* **14**, 41086–41094 (2022).
58. Li, C. et al. Non-fullerene acceptors with branched side chains and improved molecular packing to exceed 18% efficiency in organic solar cells. *Nat. Energy* **6**, 605–613 (2021).
59. Jiang, Y. et al. An alcohol-dispersed conducting polymer complex for fully printable organic solar cells with improved stability. *Nat. Energy* **7**, 352–359 (2022).
60. Dai, T. et al. Electric-induced degradation of cathode interface layer in PM7:IT-4F polymer solar cells. *Sol. RRL* **5**, 2100151 (2021).
61. Burns, S. et al. Effect of thermal annealing Super Yellsow emissive layer on efficiency of OLEDs. *Sci. Rep.* **7**, 40805 (2017).
62. Tsai, K. W. et al. Role of self-assembled tetraoctylammonium bromide on various conjugated polymers in polymer light-emitting diodes. *J. Mater. Chem. C.* **2**, 272–276 (2014).
63. Haque, S. A. et al. A multilayered polymer light-emitting diode using a nanocrystalline metal-oxide film as a charge-injection electrode. *Adv. Mater.* **19**, 683–687 (2007).
64. Wang, B. J. et al. Chain conformation control of fluorene-benzothiadiazole copolymer light-emitting diode efficiency and lifetime. *ACS Appl. Mater. Interfaces* **13**, 2919–2931 (2021).

Acknowledgements

This work was supported by grants from the National Natural Science Foundation of China (22179049) and the Jilin Provincial Department of Science and Technology (20220201067GX). Donal Bradley thanks the NEOM Education, Research, and Innovation Foundation for support.

Author contributions

J.Q. wrote the main manuscript text. Y.W. and G.W. provided {Mo132} and {Mo132}-TOA. Z.B. revised the manuscript. H.L., B.L., C.Y., and J.Z. provided experimental assistance. All authors reviewed the manuscript.

Competing interests

The authors declare no competing interests.

Additional information

Supplementary information The online version contains supplementary material available at https://doi.org/10.1038/s44406-025-00016-2.

Correspondence and requests for materials should be addressed to Jingsong Huang, Lixin Wu or Fenghong Li.